Optical Review (2020) 27:400–408
https://doi.org/10.1007/s10043-020-00620-w

SPECIAL SECTION: INVITED REVIEW PAPER

International Symposium on Imaging, Sensing, and Optical Memory (ISOM' 19), Niigata, Japan

Review paper: imaging lidar by digital micromirror device

Yuzuru Takashima[1] · Brandon Hellman[1]

Received: 16 August 2020 / Accepted: 6 September 2020 / Published online: 25 September 2020

Abstract
Applications of digital micromirror device for lidar are overviewed. A large Lagrange invariant value makes DMD as one of the attractive beam steering transmitter and receiver solutions for a time-of-flight lidar, especially with its an extended angular throw by synchronized pulsed laser illumination.

Keywords Lidar · Beam steering · Digital micromirror device · Etendue

1 Introduction

Digital micromirror device (DMD) has been around for over 30 years since its adoption to consumer projection display products [1]. DMD has been recognized as one of the key display devices along with liquid crystal displays (LCDs), liquid crystal on silicon (LCoS) displays, grating light bulbs (GLVs) and resonant mirror-based mirror scanners [2–4]. DMD modulates light by electro-mechanically actuated array of micromirrors. Dimension of each of the micromirrors is about 10 um, and they are individually and electrostatically tilted between two static states, on- and off-state [5, 6]. The on- and off-states are differentiated by tilt angle of micro mirrors, typically ± 12°, some with ± 17°, with respect to a flat state. Between the on- and off-state, there is a dynamic transitional state where micro mirrors changes its tilt angle. The dynamic motion of the micromirror is electrostatically initiated by an abrupt change of the potential difference between electrodes and micromirror itself. The initial transitional motion is assisted by a spring hinge structure implemented in the mirror yoke. The time profile of the potential difference or voltage applied to electrode and mirror enables a selective actuation of mirrors with short transitional "mirror crossover" time, which is on the order of microseconds. The short mirror crossover time enables tens of kHz binary refresh rate to increase framerate, contrast and color/grayscale bit depth of the projected image. DMDs have been applied for advanced displays, such as holographic, head mounted, near-to-eye, light field, and occluded displays [7–10]. For non-visual image display applications. DMD-based spectrometer, optical switch for optical interconnect has been reported [11, 12].

Recently, advanced autonomy for self-driving robotic cars, as well as for advanced driver assistance system (ADAS) requires new sensing and human interfaces, such as head-up display, lidar, cameras, radars and pixel light headlamp. Such optical devises for automobile have been actively researched in addition to longstanding optical devices such as headlights, interior and gauge cluster illuminations. For ADAS and robotic cars, adoption of lidar at this moment has just started. Market research shows the number of adoption of lidar units for ADAS and robotic vehicles in 2030 exceeds over 20 M units/year and will continue to grow [13]. From optical system design point of view, lidar involves complex challenges to simultaneously achieve framerate (~ 20 fps), the field of view (FOV 10–90° horizontal, 5–10° vertical), angular resolution (~ 0.1°) while satisfying requirements on eye safety, size, weight, cost, power in a harsh environment, i.e., under sunlight, vibration and temperature range of – 40 to 105 °C.

One of the fundamental challenges in lidar optics is its large Lagrange invariant (LI), known as Etendue, which is a product of angular and spatial extent of flow of energy [14]. Geometrically, LI is approximated by product of FOV

✉ Yuzuru Takashima
ytakashima@optics.arizona.edu

[1] James C. Wyant College of Optical Sciences, University of Arizona, 1630 E. University Blvd., Tucson, AZ 85720, USA

and pupil area of lidar optics. For example, one can imagine that as FOV is increased, power budgeting becomes tight for receiver optics due to the smaller entrance pupil of such wide-angle receiver optics. Similarly in lidar transmitter optics, the limited transmitter aperture area for such wide FOV optics imposes an upper limit of transmitted energy due to the limited power density for eye safety. Moreover, maximum LI is upper limited by LI of detector that affects the bandwidth of the detector. There is a complex trade-off among optics, lasers and detectors primarily dominated by LI. To work around the LI limited lidar performance, research efforts on detectors with higher sensitivity, faster readout time and arrayed format. Various lidar architecture has been proposed by employing scanning modalities including, mechanical scanners, micro electro mechanical system (MEMS) mirrors, spatial light modulators (SLMs), electrowetting, photonics crystals, slow light waveguide gratings, and optical phased arrays [13, 15–20].

In terms of the value of LI, DMD is uniquely positioned. In high-end DMD model, the array area exceeds 230 mm^2 [21]. The DMD's reflective light modulation allows to use infrared light which is commonly used for ADAS and robotic lidars. The modulation speed well exceeds that of liquid crystal-based SLM. While those distinctive nature would make DMD as potential key components for lidar.

In this review paper, we overview potentials and applications of DMD in particular for imaging lidar. Section 2 overviews radiometric aspect of lidar optical architectures. Section 3 addresses current use cases of digital micromirror devices for in lidar system. In Sect. 5, we discuss impacts of DMD's Etendue on lidar performance, especially the effect of diffraction efficiency and angular throw of newly proposed pulse synchronized operation of DMD for beam steering. Major challenges, limitations, and outlook of the research area of DMD in imaging lidar are addressed.

2 Optical architecture of lidar

A lidar system is comprised of a distance measurement mechanism and a scanning or mapping mechanism. Figure 1a schematically depicts a time-of-flight (TOF) lidar. A short laser pulse, on the order of 10 ns, is launched from a transmitter over a distance R, and is then scattered by the object back towards a receiver, typically near the transmitter. The TOF, which is used to calculate distance, is measured by high-speed electronics and a detector. Figure 1b depicts a 3-dimensional (3D) lidar system mapping distances across a 2-dimensional (2D) FOV. The system has an active scanning mechanism, such as a rotating stage or a 2D galvo mirror, or a passive mapping mechanism, such as an imaging lens with a 2D detector array. Different ranging techniques exist, such as frequency modulation, coded waveforms, heterodyne detection, and gated capture [22], but they are all dependent on the same radiometric principles.

There are two archetypal lidar architectures: (1) flash lidar, a passive image mapping using flood illumination, and (2) point-and-shoot lidar, an active 2D scanning using a collimated or 1D line beam illumination [23, 24]. In any of the lidar type, the retuning signal power P_R returned from an object is given by [23],

$$P_R = P_T \frac{\sigma A_{rec}}{A_{illum} \pi R^2} \eta_{atom}^2 \eta_{sys} \tag{1}$$

where P_T is transmitted power, σ is a cross-sectional area of an object that is upper bounded by illumination area of the transmitting beam, A_{illum}. R is a range between laser transmitter and receiver. η_{atom} and η_{sys} are the transmission of atmosphere and optical system, respectively.

2.1 Radiometry of flash, point-and-shoot, and line illumination lidar

2.1.1 Flash lidar

A flash lidar system is schematically depicted in Fig. 2a. An illumination laser 'flood' illuminates the entire FOV. A lens (not shown) images the field onto a detector array, such as an avalanche photodiode (APD) array, or alternatively onto a field selection device, such as a spatial light modulator (SLM) through which photons from a selected field-point are relayed to a single-element APD [25]. Due to the two-dimensional divergence of the illumination beam, the irradiance at the target, E_1, drops off from the irradiance at the transmitter's output aperture, E_0, as proportional to $1/R^2$, mathematically represented by $E_1 \propto (1/R^2)E_0$ [23].

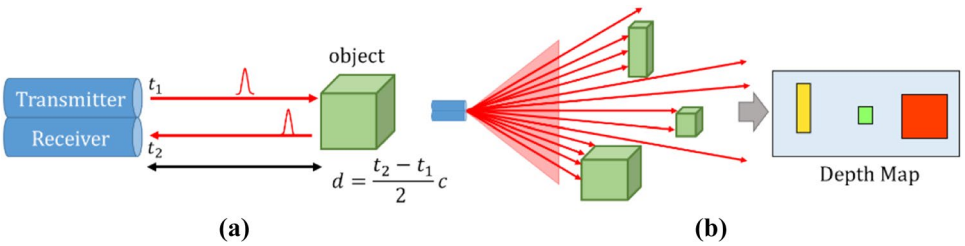

Fig. 1 **a** A time-of-flight measurement by a short laser pulse. **b** A 3D lidar system mapping distances across a 2D field-of-view

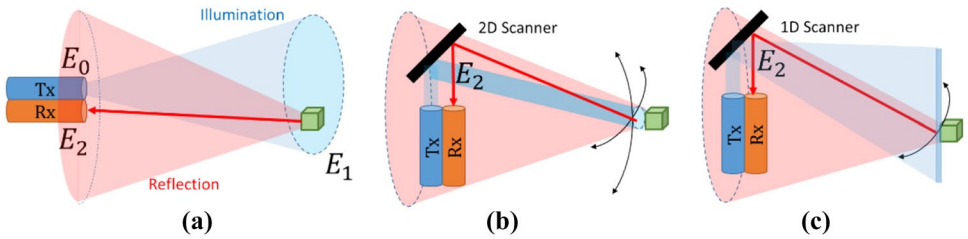

Fig. 2 **a** 2D diverging illumination. **b** Collimated illumination. **c** 1D diverging illumination

Assuming a Lambertian and diffuse reflection from the target, the irradiance returned to the collection aperture of the receiver, E_2, is given by $E_2 \propto (1/R^2)E_1 = (1/R^4)E_0$. Accordingly, this low photon efficiency has a sharp signal-to-noise ratio drop-off with distance reduces the maximum detectable distance, though the single-shot illumination (in the APD array case) is useful for high-speed captures. With a silicon photomultiplier array detector long-range detection operates in 10 Hz is reported [26]. A time-gated single-photon avalanche diode (SPAD) array with megapixel counts with an impressing frame rate of 24 kHz is reported [27].

In a flash lidar, the max range is limited by lens-dependent FOV-Entrance Pupil Diameter (EPD) tradeoff. The FOV is inversely proportional to the focal length of the lens, $f \propto (1/\text{FOV})$. However, lensing elements are F/#-limited—sometimes down to F/2.8–1.4. It follows that the FOV is inversely proportional to the diameter of the entrance pupil, FOV $\propto 1/(D_{\text{EP}})$. The returned signal is directly proportional to the area of the entrance pupil (A_{rec} in Eq. 1), or the square of the entrance pupil diameter. This is a tradeoff between signal strength and FOV.

2.1.2 Point-and-shoot lidar

A point-and-shoot lidar outputs a collimated beam improve overall photon efficiency to $E_2 \propto (1/R^2)E_0$, because of the collimated illumination makes $E_1 \sim E_0$. However, the collimated beam must be steered to each field point, a possible frame rate bottle-neck if the scanning speed is slow (often limited by slow, high-inertia mechanics). The point-and-shoot lidar is mainly adopted for 1D applications with relatively slow scan rates for consumer or robotic applications [28, 29]. Another high-end implementation for autonomous vehicle applications achieves over 100 m range with 360° [H] × 25° [V] FOV using a 1D mechanical scanning mechanism, along with multiple lasers and detectors to accommodate a vertical FOV [30]. Micro electro-mechanical system (MEMS)-based beam steering, oscillating mirrors have been demonstrated on a UAV with a range of 100 m for a particular laser power [31]. Those MEMS mirrors have resonant frequencies in the range of several kHz [32, 33]. The MEMS mirror solution, however, is limited to a 20° full FOV due to the ± 6° rotation limitation of the MEMS mirror (expanded by optics to ± 10°). The 5 mm diameter mirror is a significant limitation in the collection area of a single-aperture design and in the output aperture of single- and dual-aperture designs. The system shows the enormous speed benefits of MEMS devices due to their low inertia.

2.1.3 1D line illumination lidar

Using a 1 dimensional line illumination source is feasible along with additional field selection modality such as 1 dimensional attained detector (Fig. 2c). The horizontal dimension of the illumination beam is collimated while the vertical dimension is diverging. A 1D collimated beam has an irradiance drop-off at the target proportional to $1/R$, represented by $E_2 \propto (1/R^3)E_0$, putting the theoretical max distance cutoff in between the flash (R^{-4}) and point-and-shoot (R^{-2}) systems.

3 Use case of digital micromirror device for lidar

3.1 Holographic beam steering

A lidar employing collimated illumination or 1D diverging illumination (Fig. 2b, c) requires beams steering for transmitter and receiver. Since DMD is a binary amplitude spatial light modulator (SLM), the most straightforward method for beam steering with DMD is to project pixel patterns with a projecting lens. However, because only a fraction of mirror array is turned on, such methods suffer from a substantial reduction in power throughput.

Binary amplitude grating has in theory 10.1% of diffraction efficiency for + 1st order diffraction [34]. In a similar way to DMD-based holographic optical tweezer, beam steering by amplitude hologram is feasible [35, 36]. The full angular scan extent is rather limited and is given by $\sim \lambda/2p$ where λ is wavelength and p is pixel period. With a typical pixel period of DMD, $p = 5.4 \sim 13.8$ um and at wavelength $\lambda \sim 1$ μm, the diffraction angle is on the order of a couple of degrees which is insufficient for lidar application. That implies multiple optical channels to cover total FOV in a segmented manner is needed and discussed in Sect. 4 in detail. It is known that conservation of Lagrange invariant (Etendue) alters the area of the exit pupil (A_{rec} in Eq. 1).

Optical expansion of the angular throw by inverse telephoto optics was adopted to increase angular throw of beam steering device [37].

A binary phase hologram achieves even higher diffraction efficiency, 40% for ± 1st order diffractions when phase profile is modulated in a square wave manner between 0 and π. Although DMD is an amplitude SLM, an auxiliary optics converts DMD to a binary phase SLM [38]. Incoming plane wave to DMD is re-directed to two arms consist of catadioptic 4-f system, The 4-f optics reimages on and off pixels on top of themselves while PZT actuated mirror in of the 4-f arms adds a π phase shift. To add a π phase shift, area of DMD mirror array is halved that impacts on system LI. A higher diffraction efficiency, ~ 40%, while keeping high frame rate was demonstrated.

3.2 Beam steering with synchronized pulsed laser

Further enhancement in diffraction efficiency, 100% in theory, along with the reduction of the effective pitch of DMD was first reported in Ref. [39]. The key aspect of the approach is accessing to crossover transitions of DMD mirror array between on- and off-state. Figure 3 depicts the principle of the beam steering.

Array of micromirrors are arranged in a diamond shape, and each of micromirrors tilts ± 12° around the axis of rotation (Fig. 3a). Figure 3b illustrates the tilt angle of mirror, θ_{tilt} as a function of time. The mechanical transitional time between off- and of-sates, crossover time, is typically several μs [40]. During the crossover period, ns laser pulses illuminates mirror array in a synchronous manner to the mirror transition, i.e., at times t_1, t_2, and t_2 in Fig. 3b. Compared to the crossover time of mirror array, the ns pulse is three orders of magnitude shorter. Due to the three orders of magnitude difference of time scales, the micromirrors' movement is effectively frozen that precisely defines tilt angle of mirror array that forms a saw tooth blazed phase profile that further enhances diffraction efficiency (Fig. 3c). Between the mirror tilt angle of ± 12°, there are 5–10 tilt angles of mirrors that satisfies a blaze condition that realizes a close 100% diffraction efficiency in theory. Figure 3d illustrates a timing diagram of the beam steering operation. First, microcontroller triggers DMD (Light Crafter 3000, Texas Instruments) to initiate micromirror's movement. Prior to applying the trigger to DMD, all the micromirrors are in the off-state. For the DMD, there are about 220 μs of delay between the trigger signal and the actual micromirrors' actuation. While micromirrors are in motion from off- to on-state, ns laser pulse illuminates DMD. The illumination timing is synchronized to micromirror's motion so that the mirror tilt angle θ_{tilt} satisfies a brazed condition. The cycle is repeated for the next blazed condition to steer beam towards the next diffraction orders by adjusting the trigger to the ns laser.

The method effectively decreases the pixel period that increases LI with larger angular throw increased to about 48°. The challenge though is the number of steering point is limited to number of diffraction orders that satisfies blaze condition. Several approaches have been proposed to increase the number of scanning point. In Ref. [41], multiple laser sources with slightly different angle of incidence to single DMD were used to increase the number of scanning points. Similar approach were reported for

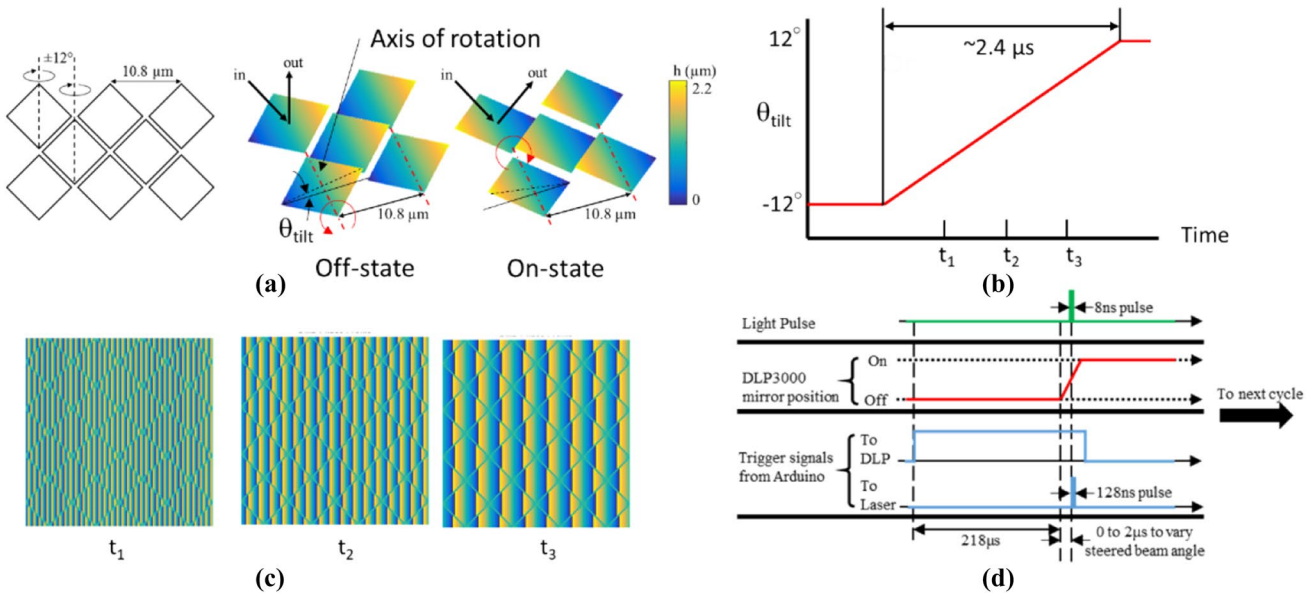

Fig. 3 **a** A "diamond" arrangement of micromirror array, (**b**) tilt angle of mirror as a function of time during the crossover period, (**c**) examples of phase profiles of micromirror array at several mirror tilt angles, and (**d**) a timing diagram of beam steering

display applications with DMD [8, 42, 43]. In Ref. [41], multiple pulses were employed within a single transition of micromirror that increases scan rate by a factor of the number of supported diffraction orders by DMD. Refs. [39] and [41] also describes benchtop demonstration of lidar systems with the beam steering approach in a single path optical architecture.

While diffraction efficiency is greatly improved by the technique, there still are challenges to apply the DMD-based beam steering technology for lidar applications, especially in number of scanning points. Reference [44] reports binary holographic beam steering is combined to the beam steering principle. Amplitude grating patterns are displayed on DMD and addressed and illuminated by a ns laser while corresponding DMD pixels representing the grating pattern is transitioning. In this way, the beam steering angle is kept large while incorporating an increased number of scanning points at the expense of reduced diffraction efficiency. With an APD detector and electronics TOF lidar is demonstrated. The beam steering principle is applied for the holographic display system with larger viewing zone [7].

3.3 Spatial filter for compressive sensing lidar

Reference [45] proposed applying single-pixel compressive sensing to TOF lidar. A 2 ns 780 nm laser diode illuminates target with 10 MHz repetition rate. The returning signal is detected by imaging lens. At the back focal plane of imaging lens, DMD is placed and spatially modulated. The modulated light is detected by photomultiplier tube (PMT). The reconstruction algorithm achieved 32×32 pixel video and 256×256 pixel still image for a sparsely placed 2D planer object within range of 0–8 m.

The combination of compressive sensing with a single photo multiplier tube (PMT) is applied to a commercially available 2D TOF sensor. Li et al. demonstrated compressive sensing improves resolution of lidar. DMD is placed at the back focal plane of the imaging lens. The image formed on DMD is modulated for compressive sensing and relayed to a 320×240 pixel commercial TOF sensor. Although the maximum range demonstrated was limited up to several meters due to the amplitude modulated continuous wave detection, the enhancement of resolution beyond physical pixel limit was demonstrated [46].

References [45, 46] report combination TOF lidar with compressive sensing. Frequency modulated continuous wave (FMCW) lidar combined with compressive sensing is reported [47]. Optical system is modelled as an ideal optics with an aperture of 2 in., and assumed that all the returning photons are captured with a detector. Simulation shows that 128×128 pixel image located at 20 m can be imaged with a single detector with DMD that employs spatial modulation of returning the signal for compressive sensing.

3.4 Adoptive spatial filtering for ambient light reduction

As Eq. (1) shows, the retuning signal power P_R from an object scales with R^{-2}, therefore, the management of environmental and stray light is critical for auto lidars targeting object at a far distance. In addition to the ambient light, interference from neighboring lidars and especially strong reflection from traffic signs impose a challenge in a dynamic range of auto lidar systems [48]. Effective and adaptive suppression of ambient light, illumination from neighboring lidars, and strong reflection from traffic signal are highly anticipated. In a similar way to confocal microscopy employing DMD as a spatial filter [49], filtering ambient light is employed by placing of DMD at the back focal plane as a spatial filter is reported [50].

Lidar system having DMD as a FOV selector/spatial filter placed back focal place of receiver lens is reported in Ref. [51]. A 1-dimentional scanner scans objects with a line illumination. The line image of the objects is formed on DMD that is placed at the back focal plane of the imaging lens. While 1-dimensional illumination scans object horizontally with vertically oriented 1D beam, DMD scans along vertical FOV. By two scanning modalities, distance is mapped to FOV. Lidar system with 5.6 fps frame rate and 50° FOV for distance measurement up to 10 m is experimentally demonstrated.

3.5 Packaging of lidar to headlight unit

Making headlight more intelligent and adoptive has been researched. Along with an active array of LED and adoptively controlling projection pattern, passive and adoptive illumination pattern generation has been proposed. DMD were employed to switch low and high beams [52]. Not only controlling the illumination pattern, a real-time capture and image processing of pedestrians, neighboring cars as well as raindrops and adoptive modulation of illumination pattern is reported [52–55]. Integration of a lidar as a part of the headlight is mentioned in Ref. [56]. The proposal is using DMD as an optical path selector switch for LED projector headlight and lidar receiver. For headlight, DMD selectively illuminates objects through projector lens. The headlight projector lens works as a lidar receiver optics by switching DMD.

4 Discussions

Key performance metrics of imaging lidar are maximum distance, the field of view (FOV), angular and distance resolution and frame rate. Reference [13] lists optical specifications of current mechanical scanning point-and-shoot lidar with a 360° horizontal FOV. The data rate spans 0.3–1.3 M samples/s for 360° FOV with multiple (16–64) transmitter/receiver channels. Interestingly, the sampling rate/degree/channel takes about the same values, 50–60 samples/s/degree/channel. This can be understood that the 360° scanning lidar extends vertical FOV by stacking multiple transmitter/receiver channels. Single-channel horizontal sampling, (framerate) × 360/(angular resolution)~22.5 k samples/s in Ref. [13]. The corresponding sampling interval, 40–50 μs, is reasonable to accommodate the time of flight as well as margins for triggering delay, and data acquisition time.

Based on the sampling rare, two lidar use case examples, forward-looking lidar for ADAS and side looking lidar for robotic cars are tabulated in Table 1. For a forward-looking lidar, full horizontal and vertical FOVs of 14 × 3.5° are assumed. The FOV corresponds to 50 × 12.3 m area at a distance of 200 m. To recognize a car with a 2 m of the extent at 200 m, with 5 sampling points, angular resolution is set to 0.1°. To achieve 30 fps under single-channel sampling rate of 22.5 kHz, 6 channels are needed. Similar analysis for a 60° horizontal FOV side looking lidar for robotic car, about the same number of optical channels ~ 5 is required.

Table 1 Use case specification of lidar for ADAS and robotic car applications

Specifications	ADAS (long range)	Robotic (side looking)
Distance (m)	200	30
FOV (H × V) (°)	14 × 3.5	60 × 5.7
Target resolution (m)	0.4 (car)	0.1 (pedestrian)
Resolution (H × V) (°)	0.3 × 0.3	0.2 × 0.2
# of samples (H × V) (pixels)	122 × 30	314 × 30
Frame rate (fps)	30	10
Sampling frequency (kHz)	112	94
# of optical channels	6 (5.6)	5 (4.7)

Table 2 summarizes benchmarking result in receiving power P_R normalized to long range ADAS for four beam steering schemes described in Sect. 3. For simplicity we have assumed, (1) object is under filled by illumination $\sigma/A_{\text{illum}} = 1$, and (2) atmospheric absorption is unity and independent to the distance for the range of 200 m. Also we have assumed a common path geometry so that the transmitter and receiver shares the same aperture area, $A_{\text{rec}} = A_{\text{trans}}$. In the analysis, power density P_T/A_{trans} for the two systems set to be equal to equalize the maximum permissible exposure as the same level among four beam steering cases. In the analysis horizontal and vertical FOVs of each of the optical channels is anamorphically adjusted to match to the native scanning extent of DMD: $\text{FOV}_{\text{DMD}} = \lambda/p \sim 7.53°$ at $\lambda = 1$ um, pixel period = 7.6 μm [57]. The receiving aperture area A_{rec} is given by,

$$A_{\text{rec}} = A_{\text{DMD}} N_{\text{opt}} N_{\text{pulse synch}} \frac{\left(\text{FOV}_{\text{DMD}}\right)^2}{\text{FOV}_{\text{h}}\text{FOV}_{\text{v}}} \tag{2}$$

where A_{DMD} is area of DMD, N_{opt} is number of optical channels, $N_{\text{pulse synch}}$ is an enhancement factor of FOV_{DMD} while employing synchronized pulse illumination, and FOV_{h} and FOV_{v} are horizontal and vertical FOV of lidar system, respectively. Also, system efficiency η_{sys} in a common path geometry is given by $\eta_{\text{sys}} = \eta_{\text{diff}}^2$, where η_{diff} is diffraction efficiency of DMD. Under that assumption, Eq. (1) is modified as,

$$P_{\text{R}} = \frac{P_{\text{T}}}{\pi}\left(\frac{A_{\text{rec}}\eta_{\text{diff}}}{R}\right)^2 \tag{3}$$

Gain factor G is defined by,

$$G = \left(\frac{P_{\text{R}}}{P_{\text{R,ADAS, Binary CGH}}}\right) \tag{4}$$

where, $P_{\text{R,ADAS, Binary CGH}}$ is a receiving power of ADAS lidar system employing binary amplitude modulation for beam steering.

Table 2 Gain factors for DMD beam steering common-path lidar for ADAS and robotic car applications

DMD beam steering case	Pulse sync. to mirror	$N_{\text{pulsesynch}}$	η_{diff}	G: ADAS (long range)	G: Robotic (side looking)
1. Binary amplitude CGH	N/A	1	0.1	1 (reference)	0.63
2. Binary phase CGH	N/A	1	0.4	2	2.53
3. Binary amplitude CGH	Applied	5	0.1	25	15.8
4. Blazed grating with scanner	Applied	5	1.0	2500	1584

Table 2 tabulates gain factor G for four beam steering schemes. The gain factor is normalized for the ADAS long-range lidar system employing binary amplitude CGH.

In this analysis, sampling rate per channel is a constant, 22.5 kHz. Under this assumption, once can see the system performance simply scales with the square of the product of Etendue of DMD ($A_{\mathrm{DMD}}N_{\text{pulse synch}}\left(\mathrm{FOV}_{\mathrm{DMD}}\right)^2$) and diffraction efficiency η_{diff}. From the system design point of view, increasing Etendue of DMD and diffraction efficiency equally contribute to lidar performance. Note that in the analysis for the case: 2. Binary phase CGH A_{DMD} is decreased by a factor of 2 to accommodate the reduction of the DMD area by factor two for phase modulation [38].

We also assumed theoretical diffraction efficiency for all the cases. The diffraction efficiency of case 3 and 4 beam steering reported in Ref. [39, 41]. Achieved ~ 40% with non-optimum coating of DMD device. The efficiency is expected to approach to 80–90% by applying an anti-reflection coating optimized for infrared spectrum. For the case 4, the blazed grating-based beam steering, the challenge is requiring an additional high-efficiency scanning modality with the Etendue to the same level of case 1, Binary amplitude CGH displayed on DMD is needed. A large resonant MEMS mirror for example 7×5 mm with $\pm 6.8°$ of scan angle, requires to achieve angular resolution requirement [15, 41]. Reference [58] reports a MEMS-based phase spatial light modulator with 0.47″ 960×540 micromirror device with an array area of 10.36×5.83 mm.

The other challenge of DMD-based beam steering is a range of distance measurement. The transitional time of micromirror is typically several microseconds. The round trip time, for example, 1us corresponds to a distance range of 150 m. In a co-axial optics where lidar transmitter and receiver shares common beam steering device, the maximum range of the DMD-based diffractive beam steering is limited by the mirror transitional time within which high diffraction efficiency is attained [41]. Electro-mechanical dynamic simulation of DMD microarray shows that the mirror transitional time increases by controlling amplitude, polarity and time profile of reset pulse [59]. Application of DMD as a spatial filter for receiver optics would be especially effective when it is combined with a camera and adoptive headlight system to select a region of interest for lidar while blocking light from neighboring lidars, sunlight and strong reflection from traffic signs. Finally, a long term evaluation of DMD-based beam steering for both static and pulse synchronized beam-steering modes is inevitable. DMD devices specifies a range of operation temperature from − 40 to + 105 °C would be a good fit for the long term evaluation [57, 60].

5 Conclusions

Digital micromirror device (DMD) has an affinity to scanning lidar system especially with its large micromirror array area. With a pulse synchronized beam steering method, the angular scanning extent increases from several degrees to several tens of degrees. Consequently, the increased space-angular extent product (Etendue or Lagrange invariant of DMD) improves photon throughout of lidar system by factor of 25 as compared to traditional beam steering with binary-amplitude computer-generated holograms. Further enhancement of photon throughput, by another factor of 100 is expected with a pulse synchronized and brazed grating mode beam steering in conjunction with high efficiency yet moderate Etendue scanning device, such as large resonant MEMS mirrors and micromirror-based phase light modulators.

Acknowledgements We acknowledge generous support by Semiconductor Research Corporation, Texas Instruments, Mitsubishi Electric, and Tech Launch Arizona on this review study of DMD-based lidar.

Funding Semiconductor Research Corporation, Texas Instruments, Mitsubishi Electric, Tech Launch Arizona.

Compliance with ethical standards

Conflict of interest Authors filed patent applications based on several articles by authors.

Availability of data and material Not applicable.

Code availability Not applicable.

References

1. Hornbeck, L.J.: Deformable-mirror spatial light modulators. Spat. Light Modul. Appl. III. **1150**, 86 (1990). https://doi.org/10.1117/12.962188
2. Bleha, W.P., Lei, L.A.: Advances in liquid crystal on silicon (LCOS) spatial light modulator technology. Disp. Technol. Appl. Def. Secur. Avion VII. **8736**, 87360A (2013). https://doi.org/10.1117/12.2015973
3. Bloom, D.M.: Grating light valve: revolutionizing display technology. Proj. Disp. **III**(3013), 165–171 (1997). https://doi.org/10.1117/12.273868
4. Urey, H.: Torsional MEMS scanner design for high-resolution scanning display systems. Opt. Scan. **4773**, 27 (2002). https://doi.org/10.1117/12.469198
5. Hornbeck, L.J.: From cathode rays to digital micromirrors: a history of electronic projection display. TI Tech. J. **15**, 7–46 (1998)
6. Hornbeck, L.J.: Digital light processing and MEMS: reflecting the digital display needs of the networked society. Micro-Opt. Technol. Meas. Sens. Microsyst. **2783**, 2–13 (1996). https://doi.org/10.1117/12.248477
7. Takekawa, Y., Takashima, Y., Takaki, Y.: Holographic display having a wide viewing zone using a MEMS SLM without pixel

pitch reduction. Opt. Express. **28**, 7392–7407 (2020). https://doi.org/10.1364/OE.385645
8. Lee, B., Yoo, D., Jeong, J., Lee, S., Lee, D., Lee, B.: Wide-angle speckleless DMD holographic display using structured illumination with temporal multiplexing. Opt. Lett. **45**, 2148 (2020). https://doi.org/10.1364/ol.390552
9. Krajancich, B., Padmanaban, N., Wetzstein, G.: Factored occlusion: single spatial light modulator occlusion-capable optical see-through augmented reality display. IEEE Trans. Vis. Comput. Graph. **26**, 1871–1879 (2020). https://doi.org/10.1109/TVCG.2020.2973443
10. Yeon-Gyeong, J., Myeong-Ho, C., Pengyu, L., Brandon, H., Lee, T.L., Yuzuru, T., Park, J.-H.: Occlusion-capable optical-see-through near-eye display using a single digital micromirror device. Opt. Lett. **45**, 3361–3364 (2020)
11. Kristensson, E., Ehn, A., Berrocal, E.: High dynamic spectroscopy using a digital micromirror device and periodic shadowing. Opt Express. **25**, 212 (2017). https://doi.org/10.1364/OE.25.000212
12. Blanche, P.A., LaComb, L., Wang, Y., Wu, M.C.: Diffraction-based optical switching with MEMS. Appl. Sci. **7**, 411 (2017). https://doi.org/10.3390/app7040411
13. The Automotive LiDAR Market. https://www.woodsidecap.com/wp-content/uploads/2018/04/Yole_WCP-LiDAR-Report_April-2018-FINAL.pdf
14. Bentley, J., Olson, C.: Field Guide to Lens Design. Society of Photo-Optical Instrumentation Engineers (SPIE), Bellingham, Bellingham (2012)
15. Mitsubishi Electric targets auto lidar with large MEMS mirror. https://optics.org/news/11/1/114
16. Bigler, C.M., Rovig, Z., McDonald, J., Blanche, P.-A.: Holographic amplification of the diffraction angle from optical phase array for optical beam steering. Appl Opt. **58**, G241 (2019). https://doi.org/10.1364/ao.58.00g241
17. Smith, N.R., Abeysinghe, D.C., Haus, J.W., Heikenfeld, J.: Agile wide-angle beam steering with electrowetting microprisms. Opt Express. **14**, 6557 (2006). https://doi.org/10.1364/OE.14.006557
18. Abe, H., Takeuchi, M., Takeuchi, G., Ito, H., Yokokawa, T., Kondo, K., Furukado, Y., Baba, T.: Two-dimensional beam-steering device using a doubly periodic Si photonic-crystal waveguide. Opt. Express. **26**, 9389 (2018). https://doi.org/10.1364/oe.26.009389
19. Ito, H., Kusunoki, Y., Maeda, J., Akiyama, D., Kodama, N., Abe, H., Tetsuya, R., Baba, T.: Wide beam steering by slow-light waveguide gratings and a prism lens. Optica. **7**, 47 (2020). https://doi.org/10.1364/OPTICA.381484
20. Poulton, C.V., Yaacobi, A., Cole, D.B., Byrd, M.J., Raval, M., Vermeulen, D., Watts, M.R.: Coherent solid-state LIDAR with silicon photonic optical phased arrays. Opt Lett. **42**, 4091 (2017). https://doi.org/10.1364/ol.42.004091
21. DLP9500UV DLP® 0.95 UV 1080p 2x LVDS Type A DMD. https://www.ti.com/document-viewer/DLP9500/datasheet/features-dlps0258119#DLPS0258119
22. Bosch, T.: Laser ranging: a critical review of usual techniques for distance measurement. Opt. Eng. **40**, 10 (2001). https://doi.org/10.1117/1.1330700
23. McManamon, P.: Field Guide to Lidar. Society of Photo-Optical Instrumentation Engineers (SPIE), Bellingham, Bellingham (2015)
24. Palmer, J.M., Grant, B.G.: Art of radiometry. SPIE, Bellingham, Bellingham (2009)
25. Itzler, M.A., Entwistle, M., Owens, M., Patel, K., Jiang, X., Slomkowski, K., Rangwala, S., Zalud, P.F., Senko, T., Tower, J., Ferraro, J.: Geiger-mode avalanche photodiode focal plane arrays for three-dimensional imaging LADAR. Proc SPIE **7808**(1), 78080C–78080C-14 (2010)
26. Kondo, S., Kubota, H., Katagiri, H., Ota, Y., Hirono, M., Ta, T.T., Okuni, H., Ohtsuka, S., Ojima, Y., Sugimoto, T., Ishii, H., Yoshioka, K., Kimura, K., Sai, A., Matsumoto, N.: A 240 × 192 Pixel 10 fps 70klux 225 m-range automotive LiDAR SoC using a 40ch 0.0036 mm^2 voltage/time dual-data-converter-based AFE. In: 2020 IEEE International solid-state circuits Conference (ISSCC). pp. 94–96. IEEE (2020)
27. Morimoto, K., Ardelean, A., Wu, M.-L., Ulku, A.C., Antolovic, I.M., Bruschini, C., Charbon, E.: Megapixel time-gated SPAD image sensor for 2D and 3D imaging applications. Optica. **7**, 346 (2020). https://doi.org/10.1364/optica.386574
28. Konolige, K., Augenbraun, J., Donaldson, N., Fiebig, C., Shah, P.: A low-cost laser distance sensor. In: 2008 IEEE International Conference on Robotics and Automation. pp. 3002–3008 (2008)
29. Okubo, Y., Ye, C., Borenstein, J.: Characterization of the Hokuyo URG-04LX laser rangefinder for mobile robot obstacle negotiation. Proc SPIE **7332**(1), 733212–7332110 (2009)
30. HDL-64E Resource Manual Laser Safety Parameters. https://www.yumpu.com/en/document/view/11660993/hdl-64e-s2-manual-velodyne-lidar
31. Kasturi, A., Milanovic, V., Atwood, B.H., Yang, J.: UAV-borne lidar with MEMS mirror-based scanning capability. In: Proc. SPIE 9832, Laser Radar Technology and Applications XXI. p. 98320M (2016)
32. Mirrorcle Technologies MEMS Mirrors Technical Overview, mirrorcletech.com
33. S12237-03P Ultra-miniture, high performance electromagnetically driven laser scanning MEMS mirror, www.hamamatsu.com
34. Goodman, J.W.: Introduction to Fourier optics. McGraw-Hill, New York (1996)
35. Curtis, J.E., Koss, B.A., Grier, D.G.: Dynamic holographic optical tweezers. Opt. Commun. **207**, 169–175 (2002). https://doi.org/10.1016/s0030-4018(02)01524-9
36. Wang, Y., Shevate, S., Wintermantel, T.M., Morgado, M., Lochead, G., Whitlock, S.: Preparation of hundreds of microscopic atomic ensembles in optical tweezer arrays. NPJ Quant. Inf. **6**, 1–5 (2020). https://doi.org/10.1038/s41534-020-0285-1
37. Zohrabi, M., Lim, W.Y., Cormack, R.H., Supekar, O.D., Bright, V.M., Gopinath, J.T.: Lidar system with nonmechanical electrowetting-based wide-angle beam steering. Opt. Express. **27**, 4404 (2019). https://doi.org/10.1364/oe.27.004404
38. Hoffmann, M., Papadopoulos, I.N., Judkewitz, B.: Kilohertz binary phase modulator for pulsed laser sources using a digital micromirror device. Opt. Lett. **43**, 22 (2018). https://doi.org/10.1364/ol.43.000022
39. Smith, B., Hellman, B., Gin, A., Espinoza, A., Takashima, Y.: Single chip lidar with discrete beam steering by digital micromirror device. Opt. Express. **25**, 14732 (2017). https://doi.org/10.1364/oe.25.014732
40. Knipe, R.L.: Challenges of a digital micromirror device: modeling and design. Proc. SPIE. **2783**(1), 135–145 (1996)
41. Rodriguez, J., Smith, B., Hellman, B., Takashima, Y.: Fast laser beam steering into multiple diffraction orders with a single digital micromirror device for time-of-flight lidar. Appl. Opt. **59**, G239 (2020). https://doi.org/10.1364/AO.393075
42. Hellman, B., Takashima, Y.: Angular and spatial light modulation by single digital micromirror device for multi-image output and nearly-doubled étendue. Opt. Express. **27**, 2147 (2019). https://doi.org/10.1364/OE.27.021477
43. Hellman, B., Lee, T.E.D., Park, J.-H., Takashima, Y.: Gigapixel and 1440-perspective extended-angle display by megapixel MEMS-SLM. Opt. Lett. **45**, 5016–5019 (2020). https://doi.org/10.1364/OL.395663
44. Hellman, B., Luo, C., Chen, G., Rodriguez, J., Perkins, C., Park, J.-H., Takashima, Y.: Single-chip holographic beam steering for lidar by digital micromirror device with angular and spatial

hybrid multiplexing. Opt. Express. **28**, 21993 (2020). https://doi.org/10.1364/oe.394114
45. Howland, G.A., Lum, D.J., Ware, M.R., Howell, J.C.: Photon counting compressive depth mapping. Opt. Express. **21**, 23822 (2013). https://doi.org/10.1364/oe.21.023822
46. Li, F., Chen, H., Pediredla, A., Yeh, C., He, K., Veeraraghavan, A., Cossairt, O.: CS-ToF: high-resolution compressive time-of-flight imaging. Opt Express. **25**, 31096 (2017). https://doi.org/10.1364/OE.25.031096
47. Lum, D.J., Knarr, S.H., Howell, J.C.: Frequency-modulated continuous-wave LiDAR compressive depth-mapping. Opt. Express. **26**, 15420 (2018). https://doi.org/10.1364/oe.26.015420
48. Shepard, H.: Predicting stray light artifacts in direct detection lidars. In: ATTR: optical technologies for autonomous cars and mobility I, (AF1M.2) CLEO 2020 (2020)
49. Martial, F.P., Hartell, N.A.: Programmable illumination and high-speed, multi-wavelength, confocal microscopy using a digital micromirror. PLoS ONE **7**, e43942 (2012). https://doi.org/10.1371/journal.pone.0043942
50. Fenske, J., Bartlett, T.: DLP® DMD Technology: LIDAR ambient light reduction, https://www.ti.com/lit/an/dlpa093/dlpa093.pdf.
51. Hellman, B., Gin, A., Smith, B., Kim, Y.-S., Chen, G., Winkler, P., McCann, P., Takashima, Y.: Wide-angle MEMS-based imaging lidar by decoupled scan axes. Appl. Opt. **59**, 28–37 (2020). https://doi.org/10.1364/AO.59.000028
52. Hung, C.C., Fang, Y.C., Huang, M.S., Hsueh, B.R., Wang, S.F., Wu, B.W., Lai, W.C., Chen, Y.L.: Optical design of automotive headlight system incorporating digital micromirror device. Appl. Opt. **49**, 4182–4187 (2010). https://doi.org/10.1364/AO.49.004182
53. Farris, J., Ballard, B.: Trends in high resolution headlamps. 1–19 (2019)
54. Günther, A.: Optical concept for an active headlamp with a DMD array. Opt. Sens. **7003**, 70032D (2008). https://doi.org/10.1117/12.782071
55. Wolf, A., Kloppenburg, G., Danov, R., Lachmayer, R.: DMD based automotive lighting unit. In: DGaO Proceedings (2016)
56. Li, K., Peng, Y.: Single DMD Intelligent Headlight with LiDAR. In: Proc. SPIE 11294, Emerging Digital Micromirror Device Based Systems and Applications XII. p. 112940H (2020)
57. DLP5531-Q1 0. 55-Inch 1.3-Megapixel DMD for Automotive Exterior Lighting, https://www.ti.com/lit/ds/symlink/dlp5531-q1.pdf?ts=1597595243454.
58. Bartlett, T.A., McDonald, W.C., Hall, J.N.: Adapting Texas instruments DLP technology to demonstrate a phase spatial light modulator. In: Proc. SPIE 10932, Emerging Digital Micromirror Device Based Systems and Applications XI. pp. 109320S-109320S–13. SPIE (2019)
59. Long, R.: Via integrity effects on DMD pixel dynamics. Texas Tech University (2004)
60. Yu, T.: Accelerated aging of the digital micromirror device using full custom electrostatic control. Texas Tech University (2004)